Coupled Digital Image Correlation and Peridynamics for Full-Field Deformation Measurement and Local Damage Prediction

Tianyi Li[1], Xin Gu[1] , Qing Zhang[1, *] and Dong Lei[1]

Abstract: Digital image correlation (DIC) measurement technique and peridynamics (PD) method have been applied in specific fields extensively owing to their respective advantages in obtaining full-field deformation and local failure of loaded materials and structures. This study provides a simple way to couple DIC measurements with PD simulations, which can circumvent the difficulties of DIC in dealing with discontinuous deformations. Taking the failure analysis of a compact tension specimen of aluminum alloy and a static three-point bending concrete beam as examples, the DIC experimental system firstly measures the full-field displacements, and then the PD simulation is applied on potential damage regions determined according to the correlation coefficients, to track the micro-crack evolution and macro-crack propagation. As results, the coupled DIC and PD approach can effectively measure the full-field displacement and the localized damage accumulation and crack propagation.

Keywords: Digital image correlation, peridynamics, discontinuity, damage.

1 Introduction

The Digital Image Correction (DIC) is a non-contact technique for measuring the full-field displacement of loaded materials and structures [Sutton, Wolters, Peters et al. (1983)]. Specifically, the digital cameras are used to track and record a series of speckle images of the specimen surface during deformation, then the image correlation matching algorithms [Lei, Hou and Gong (2012); Chu, Ranson and Sutton (1985); Caggegi, Chevalier, Pensée et al. (2016)] applied to pixel points in the digital images are adopted to determine the full-field displacement. As a full-field and non-contact measurement technique, DIC has gained great popularities in applications of various materials, such as metals [Cai, Zhang, Yang et al. (2016); Tung, Shih and Kuo (2010); Pan, Yu and Wu (2015)], concrete [Jiang, Jin, Zhao et al. (2017); Lei, Yang, Xu et al. (2017)], polymers [Grytten, Daiyan, Polanco-Loria et al. (2009); Jerabek, Major and Lang (2010)] and biomaterials [Murienne, Chen, Quigley et al. (2016)]. As it is known, most DIC methods are based on the

---

[1]Department of Engineering Mechanics, Hohai University, Nanjing, China.
*Corresponding Author: Qing Zhang. Email: lxzhangqing@hhu.edu.cn.

optical flow theory, whose accuracy is depended on the smoothness of displacement. Specifically, the DIC can accurately and effectively measure the continuous deformation, while its measured displacement is inaccurate or even problematic for the regions with non-smooth, discontinuous displacement or with severe noise. To improve the accuracy of DIC results with non-smooth or discontinuous deformation, many scholars have proposed some advanced strategies. Such as applying the extended finite element method in DIC simulation [Réthoré, Hild and Roux (2008); Lall, Kulkarni, Angral et al. (2010)], coupling the wavelet packet transform and DIC [Lei, Yang, Xu et al. (2017)] or directly extending standard DIC method [Réthoré, Roux and Hild (2007); Poissant and Barthelat (2010)]. However, obtaining accurate deformation measurements involving discontinuities still remains challenging. As an alternative improvement, Conradie et al. [Conradi, Turner and Becker (2014)] first characterized damage evolution in a graphite double torsion tests by using the bond-based peridynamics (BB PD) based on the DIC measured displacement. Later, in order to obtain the global displacement and local damage information of a graphite material, Turner [Turner (2014)] combined the traditional DIC measured continuous deformation results with the deformation and damage results of discontinuous regions predicted by the ordinary state-based peridynamics (OSB PD). This method take advantage of peridynamics in simulating the simultaneous of multiple cracks propagation without the requirements for external crack nucleation and propagation criteria, also prior crack locations and crack paths.

Peridynamic theory, proposed by Silling, is a nonlocal reformulation of classical continuum mechanics [Silling (2000)]. PD motion equations of a material point of interest are based on the integration of pairwise force of bonds between material points within a surrounding region, not involving any spatial derivatives of the displacement components. There are three types of PD models, respectively as the BB PD [Silling and Askari (2005); Silling, Epton, Weckner et al. (2007)], the OSB PD [Silling, Epton, Weckner et al. (2007); Le, Chan and Schwartz (2014)] and the non-ordinary state-based peridynamics (NOSB PD) [Silling, Epton, Weckner et al. (2007); Warren, Silling, Askari et al. (2009); Gu, Madenci and Zhang (2018)]. The BB PD, a special case of the OSB PD, is widely used for cracking and fracture simulations; however, it only takes the dilatation deformation state into consideration, leading to a fixed Poisson's ratio limitation [Silling, Epton, Weckner et al. (2007); Le, Chan and Schwartz (2014); Warren, Silling, Askari et al. (2009); Gu, Madenci and Zhang (2018); Gu, Zhang and Xia (2017)]. Fortunately, the OSB PD and NOSB PD models can break through these limitations and describe complex material responses. The core concept of state-based (SB) PD is the state operator, which can be nonlinear and discontinuous. The distinct difference between the OSB PD and the NOSB PD is whether the force vector state between two material points acts along the deformation vector state or not. Recently, the OSB PD has attracted increasing interest because it can break the aforementioned limitations and do not encounter numerical oscillation problem in NOSB PD simulations. The crack propagation and fracture of various materials and structures were simulated, such as an epoxy plate with non-uniform holes [Gu, Zhang and Xia (2017)], plexiglass plate

[Dipasquale, Sarego, Zaccariotto et al. (2017)], rock-like material [Zhou, Shou and Berto (2018), single-layer graphene sheets [Liu, He, Wang et al. (2018)], Kalthoff-Winkler impact test of steel [Imachi, Tanaka, Bui et al. (2019)], concrete beam, laminated composites [Gao and Oterkus (2019)], biomaterial beams [Zhang and Qiao (2018)] and etc. In addition, Han et al. [Han, Lubineau, Azdoud et al. (2016)] developed a morphing method for coupling the classical continuum mechanics model and OSB PD model, and Bie et al. [Bie, Cui and Li (2018)] coupled OSB PD with node-based smoothed finite element method (NS-FEM) to investigate crack propagation. These investigations demonstrated that the OSB PD is reliable for dynamic crack propagation prediction involving micro- and macro- cracks.

The invisibility of micro-cracks makes it challenging for DIC algorithm to recognize and display them, and the discontinuity of micro-cracks and macro-cracks results in that DIC cannot accurately capture the discontinuous displacement as well. Therefore, taking the advantages of OSB PD for crack initiation and propagation modeling regardless of material continuity, an integrated approach of DIC and PD to obtain full-field displacement and local damage of loaded materials is possible. For this end, this paper is organized as follows: Section 2 describes the equations for OSB PD modeling, Section 3 introduces the basic principles of DIC; then an integrated DIC and OSB PD approach is proposed to obtain the full-field displacement and local damage in Section 4. Section 5 validates this approach through two representative tests, i.e., a compact tension specimen of aluminum alloy and a static three-point bending concrete beam. Conclusions are drawn in Section 6.

2 Ordinary state-based peridynamics

2.1 Governing equation and constitutive model

Peridynamics regards materials as a composition of massive material points with finite volume and mass. There are nonlocal interactions spanning a certain length scale among material points, therefore, the integral form of motion equations of a material point of interest, **x** (call source point), can be derived as [Silling, Epton, Weckner et al. (2007)]

$$\rho\left(\mathbf{x}\right)\ddot{\mathbf{u}}\left(\mathbf{x},t\right)=\int_{H_{\mathbf{x}}}\left\{\underline{\mathbf{T}}\left[\mathbf{x},t\right]\left\langle\mathbf{x}'-\mathbf{x}\right\rangle-\underline{\mathbf{T}}\left[\mathbf{x}',t\right]\left\langle\mathbf{x}-\mathbf{x}'\right\rangle\right\}dV_{\mathbf{x}'}+\mathbf{b}(\mathbf{x},t), \tag{1}$$

where ρ is the mass density, $\ddot{\mathbf{u}}$ is the acceleration, $\mathbf{b}$ is specified body force density, $dV_{\mathbf{x}'}$ is the infinitesimal volume of material point $\mathbf{x}'$, which can be called the family member of point **x**, as shown in Fig. 1. Denote $\int_{H_{\mathbf{x}}}\left\{\underline{\mathbf{T}}\left[\mathbf{x},t\right]\left\langle\mathbf{x}'-\mathbf{x}\right\rangle-\underline{\mathbf{T}}\left[\mathbf{x}',t\right]\left\langle\mathbf{x}-\mathbf{x}'\right\rangle\right\}dV_{\mathbf{x}'}$ as $\mathrm{L}\left(\mathbf{x},t\right)$, representing the total force density of point **x**. $H_{\mathbf{x}} = H(\mathbf{x},\delta) = \{\mathbf{x}'\in R:\{\|\mathbf{x}'-\mathbf{x}\|\leq\delta\}\}$ represents the nonlocal integration domain of the source point with its horizon radius of δ, $\underline{\mathbf{T}}\left[\mathbf{x},t\right]$ and $\underline{\mathbf{T}}\left[\mathbf{x}',t\right]$ are the force vector states at the point **x** and $\mathbf{x}'$, and the angle bracket $\langle\rangle$ indicates the vector the force state operates on.
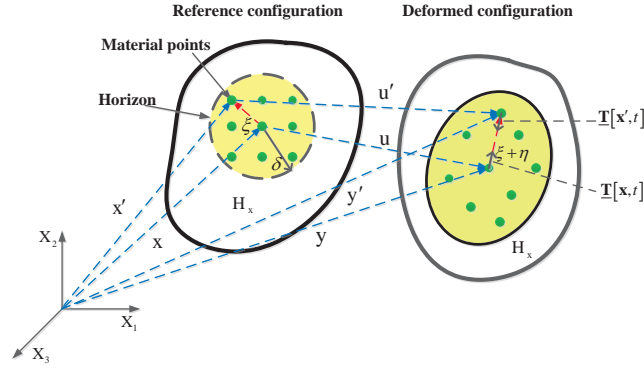
Figure 1: Schematic of interaction between peridynamic material points

The constitutive relationship denoted with force vector state as $\underline{\mathbf{T}} = \underline{\mathbf{T}}(\underline{\mathbf{Y}})$, can be simplified into the corresponding scalar state as $\underline{t} = \underline{t}(\underline{e}) = \underline{t}(\theta, \underline{e}^d) = \underline{t}(\underline{e}^i, \underline{e}^d)$, and specifically as

$$\underline{t}(\underline{e}) = \begin{cases} \underline{t}(\theta, \underline{e}^d) = \left[\frac{\gamma k}{m} - \frac{(3-\gamma)\alpha}{9}\right]\omega\theta\underline{x} + \alpha\omega\underline{e}^d \\ \underline{t}(\underline{e}^i, \underline{e}^d) = \left[\frac{3\gamma k}{m} - \frac{(3-\gamma)\alpha}{3}\right]\omega\underline{e}^i + \alpha\omega\underline{e}^d \end{cases}, \tag{2}$$

where $\underline{t}$ is a force scalar state, which can be decomposed into the isotropic component $\underline{t}^i$ and the deviatoric component $\underline{t}^d$, $\underline{e}^i$ and $\underline{e}^d$ are the isotropic component and deviatoric component of the extension scalar state $\underline{e}$, which is defined as $\underline{e} = |\mathbf{y}' - \mathbf{y}| - |\mathbf{x}' - \mathbf{x}|$. The reference relative position vector ξ between point $\mathbf{x}$ and $\mathbf{x}'$ is $\xi = \mathbf{x}' - \mathbf{x}$, and the deformed positions are specified by $\mathbf{y} = \mathbf{x} + \mathbf{u}$ and $\mathbf{y}' = \mathbf{x}' + \mathbf{u}'$ with $\mathbf{u}$ and $\mathbf{u}'$ denoting their displacements. $\underline{x} = |\mathbf{x}' - \mathbf{x}| = |\xi|$ is the initial deformation scalar state, ω is an influence function which only depends on the bond length $|\xi|$ [Silling, Epton, Weckner et al. (2007)]. For plane stress problem, the parameter γ equals $\frac{2(2\mu-1)}{\mu-1}$, where μ is the Poisson's ratio. k and α are related to the bulk modulus K and shear modulus G as $k = K + \frac{G(\mu+1)^2}{9(2\mu-1)^2}$ and $\alpha = \frac{8G}{m}$, where m is a weighted volume defined as $m = \omega\underline{x} \bullet \underline{x} = \int\limits_{H_{\mathbf{x}}} \omega(|\xi|)|\xi|^2 dV_{\mathbf{x}'}$.

Furthermore, the dilatation scalar state can be defined as $\theta(e) = \gamma\frac{(\omega\underline{x}) \bullet \underline{e}}{m}$, and the isotropic component of the extension scalar state is expressed as $\underline{e}^i = \frac{\theta\underline{x}}{3}$.

In order to analyze the strain state, the peridynamic differential operator (PDDO) [Gu, Madenci and Zhang (2018); Madenci, Barut and Futch (2016); Madenci, Dorduncu, Barut et al. (2017); Gu, Zhang and Madenci (2019)] is introduced to define the nonlocal deformation gradient tensor,

$$\mathbf{F}(\mathbf{x}) = \int_{H_\mathbf{x}} (\mathbf{y}' - \mathbf{y}) \otimes \mathbf{g}\left(\xi; N\right) dV_{\mathbf{x}'}, \tag{3}$$

where the symbol $\otimes$ denotes the dyadic product of two vectors, N is the order of Taylor series expansion (TSE), the vector $\mathbf{g}$ is composed of PD functions described by Madenci et al. [Madenci, Barut and Futch (2016); Madenci, Dorduncu, Barut et al. (2017); Gu, Zhang and Madenci (2019)] as $\mathbf{g}\left(\xi; N\right) = \left\{ \begin{array}{ccc} g_N^{100}(\xi) & g_N^{010}(\xi) & g_N^{001}(\xi) \end{array} \right\}^T$.

Furthermore, approximating the nonlocal deformation gradient tensor as a corresponding local one, the Green strain tensor is given by

$$\mathbf{E} = \frac{1}{2}\left(\mathbf{F}^{\mathrm{T}}\mathbf{F} - \mathbf{I}\right). \tag{4}$$

2.2 Numerical implementation

Explicit time integrations are suitable for solving PD motion equations to model large deformation with evolving discontinuities. In the reference configuration, a body is uniformly discretized into particles with a certain volume [Silling and Askari (2005); Parks, Seleson, Plimpton et al. (2011); Huang, Lu and Qiao (2015)], the integral-differential equation of motion can be formulated as

$$\rho\ddot{\mathbf{u}}_i^n = \sum_p \left\{ \mathbf{\underline{T}}\left[\mathbf{x}_i^n, t\right]\left\langle \mathbf{x}_p^n - \mathbf{x}_i^n \right\rangle - \mathbf{\underline{T}}\left[\mathbf{x}_p^n, t\right]\left\langle \mathbf{x}_i^n - \mathbf{x}_p^n \right\rangle \right\} V_p + \mathbf{b}(\mathbf{x}_i^n), \tag{5}$$

where n denotes the number of time step. V_p is the involved volume of material point $\mathbf{x}_p$. $\sum$ is the summation notation. $\ddot{\mathbf{u}}_i^n$ and $\ddot{\mathbf{u}}_i^{n+1}$ is the acceleration of point $\mathbf{x}_i$ at time t_n and t_{n+1}, respectively. The displacement of point $\mathbf{x}_i$ at time t_{n+1} can be obtained with an explicit Verlet-Velocity difference formula [Parks, Seleson, Plimpton et al. (2011)].

$$\begin{aligned} \dot{\mathbf{u}}_i^{n+1} &= \dot{\mathbf{u}}_i^n + \frac{\Delta t}{2\rho}\left[(\mathbf{L_u} + \mathbf{b})^n + (\mathbf{L_u} + \mathbf{b})^{n+1}\right] \\ \mathbf{u}_i^{n+1} &= \mathbf{u}_i^n + \dot{\mathbf{u}}_i^n \Delta t + \frac{(\Delta t)^2}{2\rho}(\mathbf{L_u} + \mathbf{b})^n \end{aligned}. \tag{6}$$

2.3 Damage evolution with bond breakage criterion

The crack initiation, propagation and coalescence represented by damage evolution is modeled via the permanent rupture of bonds. In order to specify whether a bond is broken or not, a history-dependent scalar-valued function, μ, that takes on values of either 1 or 0 is introduced [Silling and Askari (2005)]

$$\mu(\xi, t) = \left\{ \begin{array}{ll} 1 & \text{if } s < s_0 \\ 0 & \text{if } s \geq s_0 \end{array} \right., \tag{7}$$

where the elongation s of a bond means the relative displacement between material points, each bond breaks and does not contribute to interactions if the elongation exceeds a given critical value of s_0. During the deformation, the material is considered to be perfectly micro-elastic until it exceeds the critical stretch. The damage measure of a material point can be defined as the ratio of the number of broken bonds to the number of bonds in the horizon, and as follows:

$$\varphi(\mathbf{x}, t) = 1 - \frac{\int\limits_H \mu(\mathbf{x}, t, \xi) dV_{\mathbf{x}'}}{\int\limits_H dV_{\mathbf{x}'}}. \tag{8}$$

The damage value ranges from 0 to 1. When $\varphi(\mathbf{x}, t) = 1$, all the bonds connected to the material point $\mathbf{x}$ are broken, when $\varphi(\mathbf{x}, t) = 0$, all the bonds are intact. The presence of a crack is indicated by a damage value of about 0.5. Because the material response is dependent on the damage state, all the bond stretch needs to be checked at each step.

3 Digital image correlation

The correlation criteria of standard DIC use Normalised Sum-Squared Difference (NSSD) algorithm to correlate the changes of pixels in a deformed image compared to the reference image [Chu, Ranson and Sutton (1985)]. The correlation coefficient is defined as

$$C = 1 - \frac{\sum\sum \left[f(x, y) - \bar{f}\right]\left[h(x*, y*) - \bar{h}\right]}{\sqrt{\sum\sum \left[f(x, y) - \bar{f}\right]^2 \sum\sum \left[h(x*, y*) - \bar{h}\right]^2}}, \tag{9}$$

where C is the cross-correlation coefficient; $f(x, y)$ is the greyscale value of the pixel intensity at the point (x, y) in the reference image, whose value range is $[0, 255]$, $\bar{f}$ is the average grayscale of the corresponding subdomain, $h(x*, y*)$ is the grayscale value of point $(x*, y*)$ on the target graph, $\bar{h}$ similarly is the average grayscale of the corresponding sub-region.

It is noteworthy that DIC correlates square subdomains that comprise of a wide variation of greyscale pixels and can be distinguished from other subdomains. Generally, the reference image is discretized with subdomains with a size of $(2M + 1) \times (2M + 1)$ and a central position (x, y), then the correlation algorithm combined with the marching technique applied on the target images to find out the corresponding deformed subdomains matching to the reference subdomains.

The displacement and new position are calculated by the distance between the control point of a template image and the centroid of a target image with the correlation algorithm to

maximize the correlation coefficient C, and then the displacement gradients can be obtained through the following formulas.

$$x* = x + u + \frac{\partial u}{\partial x}\Delta x + \frac{\partial u}{\partial y}\Delta y, \tag{10}$$

$$y* = y + v + \frac{\partial v}{\partial x}\Delta x + \frac{\partial v}{\partial y}\Delta y, \tag{11}$$

where u and v are the displacement components of the reference image center (x, y) in coordinate directions, Δx and Δy are the distances from point $(x*, y*)$ to the center (x, y) of the reference computational window, and $\frac{\partial u}{\partial x}, \frac{\partial u}{\partial y}, \frac{\partial v}{\partial x}, \frac{\partial v}{\partial y}$ are the displacement gradient components of the subdomain.

4 Coupled DIC and peridynamics

We target to address the difficulties of DIC in both tracking the damage evolution and accurately capturing the local displacement around discontinuities by using the OSB PD in local damage regions. This new method of coupling DIC and PD is based on Turner algorithm [Turner (2014)], and the discrepancy is that our method can deal with complex experiments better and has higher computational efficiency in areas with the low correlation coefficient. When we deal with this case, the results are only acquired by PD simulation, while the Turner algorithm needs to combine PD and DIC results.

Firstly, as with any DIC method, multiple control points are established in the reference image and discretized by subdomains (Fig. 2(a)). Secondly, the correlation between target subdomains in the deformed image and the reference subdomains is evaluated using a correlation algorithm (Fig. 2(b)). Then, the local subdomains with poor correlation coefficient, such as *C*<0.9, are recognized as damage regions (Fig. 2(c)), which will be further analyzed by peridynamics. It is noteworthy that the picked damage region had better occupy a regular shape. The highly accurate DIC displacements of points surrounding the picked damage regions are set as displacement boundary conditions (BC) [Oterkus, Madenci, Weckner et al. (2012)], as shown in Fig. 2(d). To conduct peridynamic simulations, the meshfree particle method is adopted to discretize the damage regions into a set of material points with characteristic volume. When using uniform orthogonal discretization (Fig. 2(e)), the grid spacing between PD material points should be shorter than that between DIC control points for more accurate results. Finally, the displacement distribution and local damage in these regions can be captured by the PD analysis, as displayed in Fig. 2(f).

In the present approach, mechanics and DIC are decoupled, so that the analyst can use any DIC approach appropriate to obtain global displacements of problems and use PD to obtain local displacements and damages for areas that DIC does not work accurately.
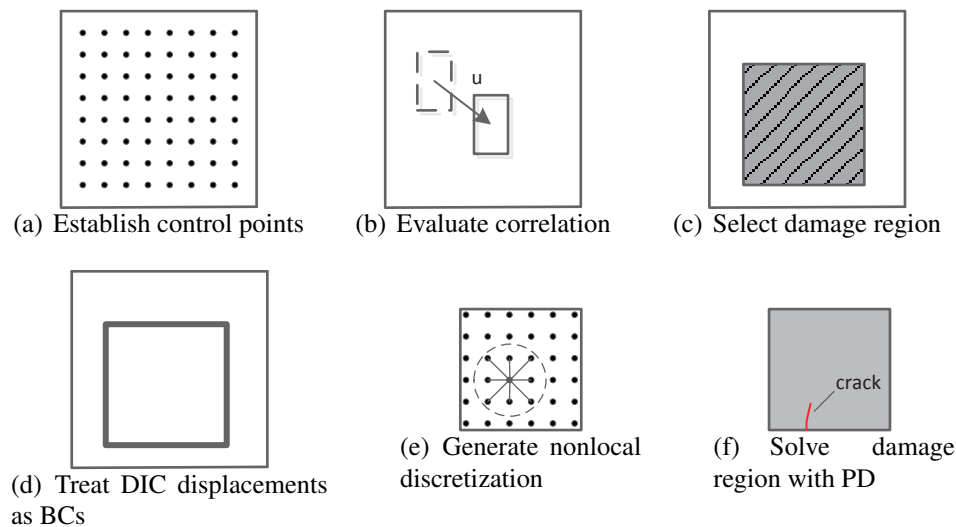
(a) Establish control points   (b) Evaluate correlation   (c) Select damage region

(d) Treat DIC displacements as BCs   (e) Generate nonlocal discretization   (f) Solve damage region with PD

Figure 2: General overview of the steps involved in the coupled DIC and PD algorithm

5 Numerical examples and results

5.1 Compact tension test of aluminum alloy

In order to validate the capability of the integrated DIC and PD method, a compact tension specimen test was performed on aluminum alloy [Justin and Antonia (2015)] as shown in Fig. 3(a). It should be noted that a DIC method without any subpixel accuracy or advanced sophistication was selected to show that the integration method works well even for a simple DIC method. The spacing of DIC control point is set as 5 pixels, which is identical to 5 mm in actual specimens. Moreover, the Young's modulus, Poisson's ratio and yield stress are respectively as $E = 70\ GPa$, $\nu = 0.32$ and $\sigma_Y = 245\ MPa$ [Farahani, Tavares, Belinha et al. (2018)]. A two-dimensional OSB PD calculation model is established for the red box area as shown in Fig. 3(b). Specifically, the critical stretch is 0.01. the grid spacing of material points is chosen as Δx=2.5 mm the horizon size is set as $\delta = 3\ \Delta x$, and the time step is adopted as $\Delta t = 1 \times 10^{-7}\ s$ in the explicit time integration algorithm.

Fig. 4 shows the damage distribution or crack trajectory at three loading stages. Besides, Fig. 5 presents the discontinuous displacements after loading, from which the crack path can also be observed and be found to be coincident with the damage distribution in Fig. 4(c). Therefore, it verifies that the damage index defined in Eq. (8) is valid for representing crack paths.

The crack trajectory observed in the experiment is illustrated in Fig. 3(c). Fig. 6 shows the similarity of crack trajectories from PD numerical prediction and experimental observation, indicating that the coupled DIC and PD algorithm can identify crack locations robustly, which in turn can guide the arrangements, i.e., position and density, of DIC control points to obtain higher precision. This feature is particularly advantageous because the
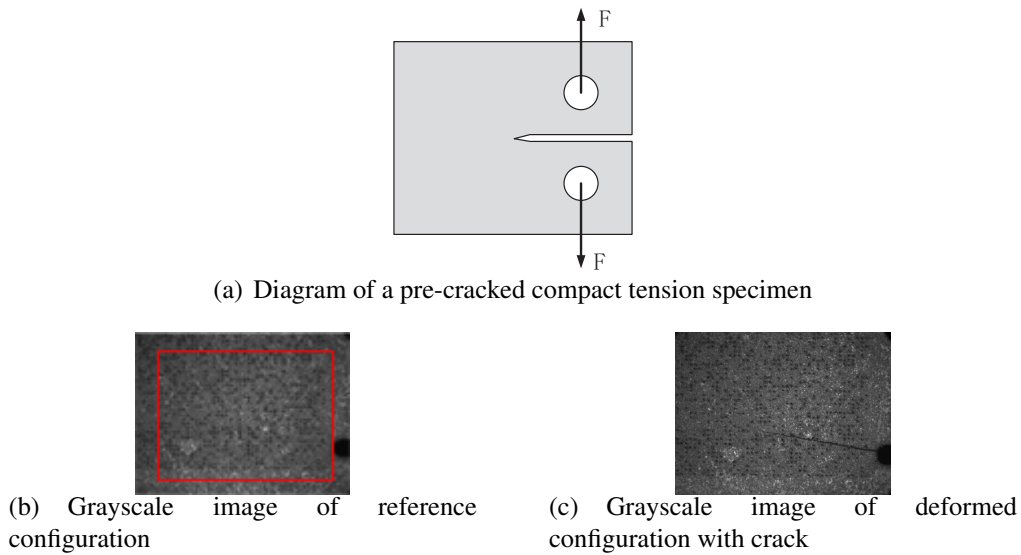
(a) Diagram of a pre-cracked compact tension specimen

(b) Grayscale image of reference configuration

(c) Grayscale image of deformed configuration with crack

Figure 3: Diagram of a compact tension specimen of aluminum alloy and grayscale images in DIC measurements

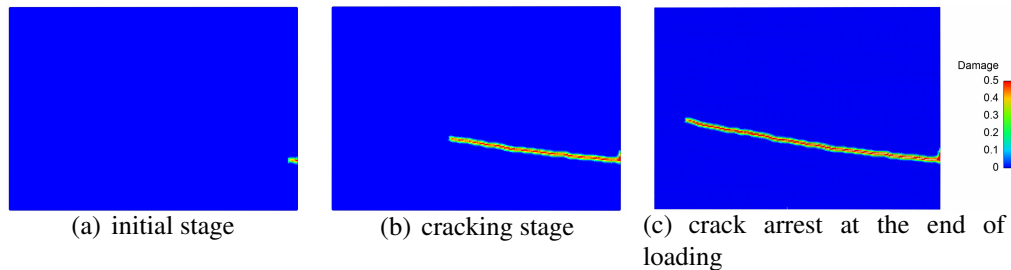
(a) initial stage

(b) cracking stage

(c) crack arrest at the end of loading

Figure 4: Damage distribution of the aluminum alloy specimen at different loading stages

microcracking locations in materials are not always identifiable with DIC method.

In addition, the PD strain components are compared with the local strain components from DIC technique, as shown in Fig. 7. The PD strains outside the crack are comparable with the local strains, while the PD strains near and inside the crack are different from the DIC results. The non-smooth and diffuse strain distribution inside the crack illustrates that PD can describe the localized deformation and failure allowing the discontinuous deformation due to its nonlocal feature.

5.2 Static three-point bending concrete beam test

5.2.1 Experiment setup of static three-point bending test

There exists a need to better quantify the failure properties of concrete due to its significance in engineering structures, so that we conducted the static three-point bending tests of
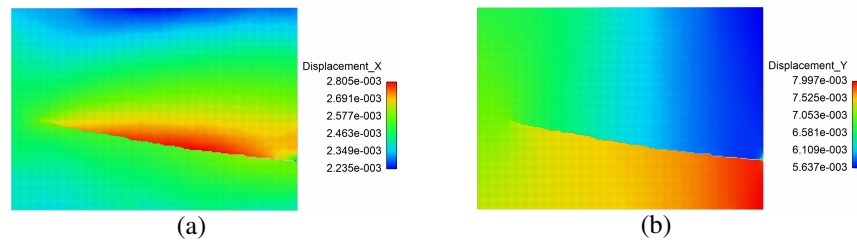
Figure 5: Full-field horizontal and vertical displacements of damaged aluminum alloy specimen
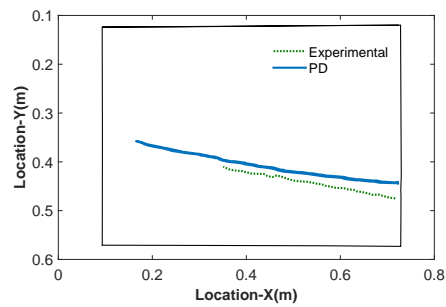

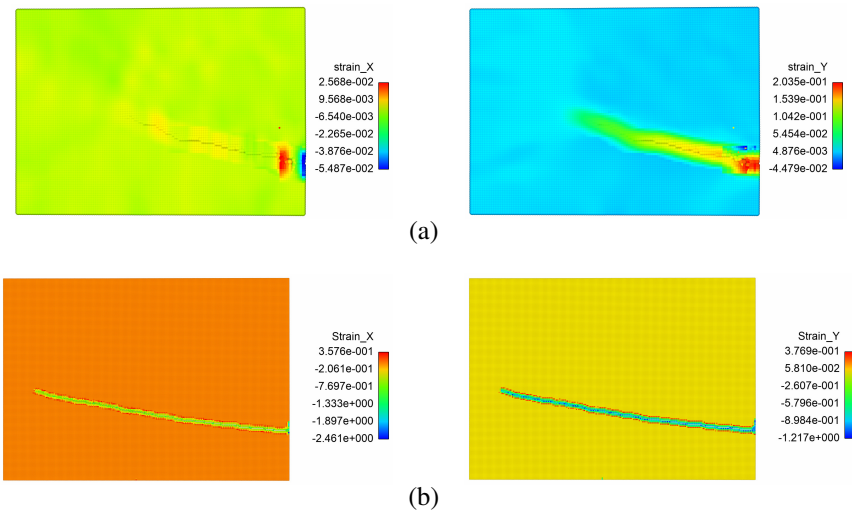**Figure 6:** Numerical and experimental crack trajectories

Figure 7: Comparison of strains in damaged aluminum alloy specimen from (a) DIC measurement and (b) PD predictions
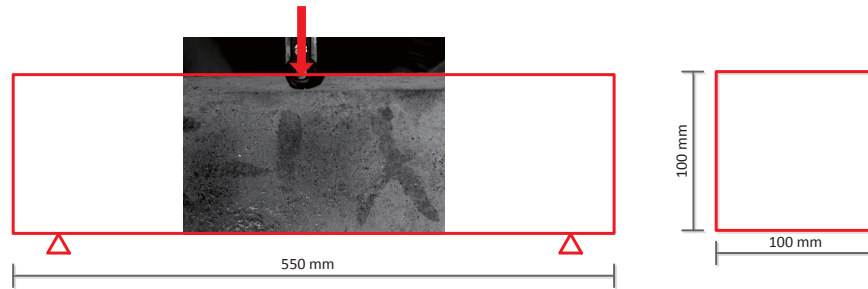
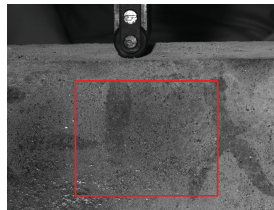**Figure 8:** Schematic diagram for the static three-point bending test of concrete beam

Figure 9: Original reference image of the concrete beam surface

concrete beams. As shown in Fig. 8, the plain concrete beam has a length of 550 mm with a square cross-section of 100 mm $\times$ 100 mm. A concentrated line load is applied at the middle of the upper surface, through the 100 kN electronic universal testing machine of CSS44100 manufactured by Changchun Testing Machine Research Institute. The concrete specimen did not break until the bending load reached to 10.08 kN. The DIC acquisition system collected 504 images of this three-point bending beam during the loading process. However, it is difficult for a DIC system to capture the micro-cracks evolution before they become visible. As mentioned in the introduction, although several improvement strategies have been proposed to compensate this shortcoming, it is still difficult to capture the unguided crack paths.

5.2.2 Characteristics of fracture process

Because cracks primarily occur in the middle of the bottom surface with maximum tensile stress state in the three-point bending test, the DIC technique targets to the red box region as shown in Fig. 9 and arranges a set of control points in it. The correlation criterion is applied on the deformed images suffering different load levels, to evaluate the corresponding cross-correlation coefficients as depicted in Fig. 10. The red areas with cross-correlation coefficient of $C = 1$ indicate that the target images are matching well with the reference image. The blue areas represent the lower correlation between the target image and the reference image. As shown in Fig. 11(c), the crack in the specimen cannot be detected by our naked eyes, although the cross-correlation coefficients especially in local blue region in Fig. 10(b) has suggested the lower correlation, representing the possibility of discontinuous deformation and cracking.
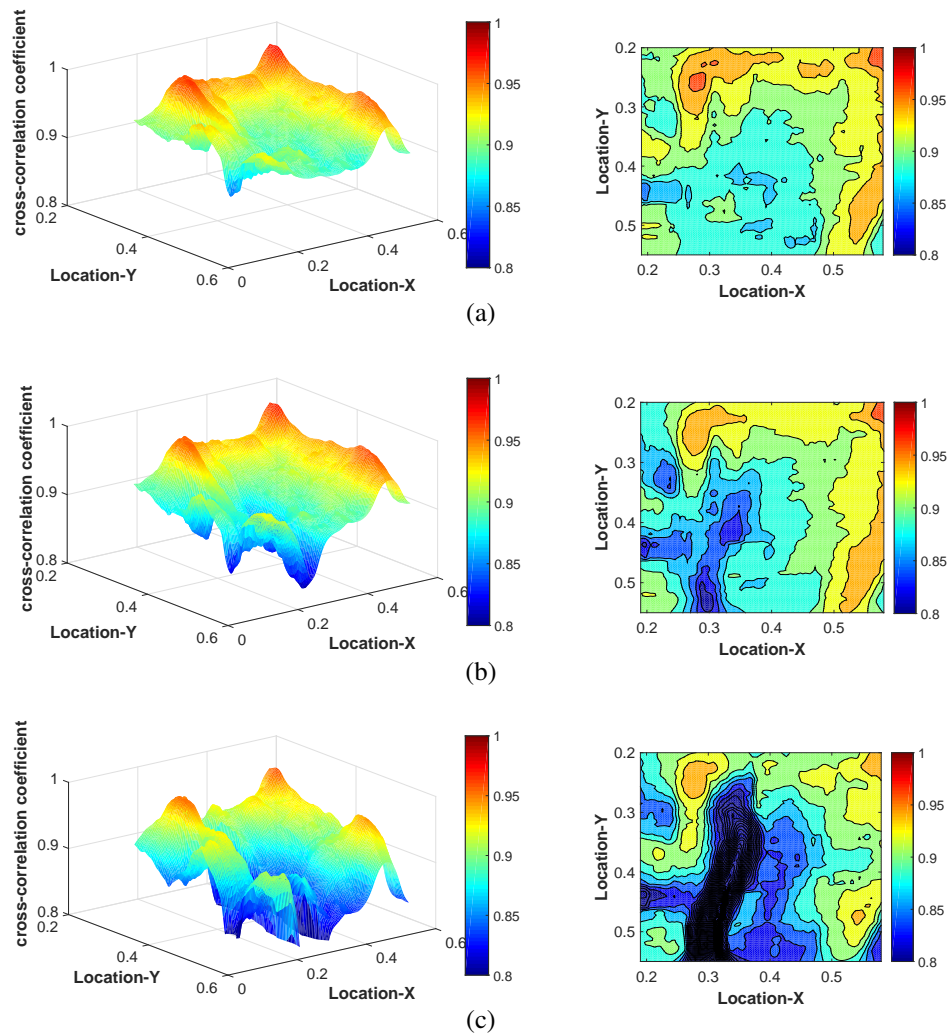
(a)

(b)

(c)

Figure 10: Cross-correlation coefficient distribution of deformed images under different loading level of (a) 3.34 kN, (b) 7.78 kN and (c) 10.00 kN

Table 1: Parameters used in this problem

Parameter	Elastic modulus	Poisson's ratio	Density	Horizon	Image size	Template size
Value	30 GPa	0.25	2350 Kg/m^3	$3 \times$ cell radius	1624×1224 pixels	5×5 pixels
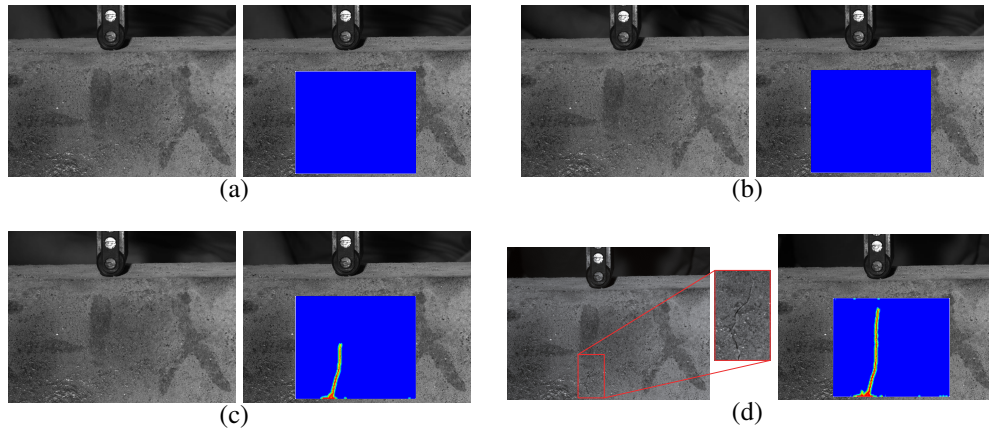
Figure 11: Surface morphologies from DIC and PD predicted damage distribution under the loads of (a) 0 kN, (b) 3.34 kN, (c) 7.78 kN, and (d) 10.00 kN respectively
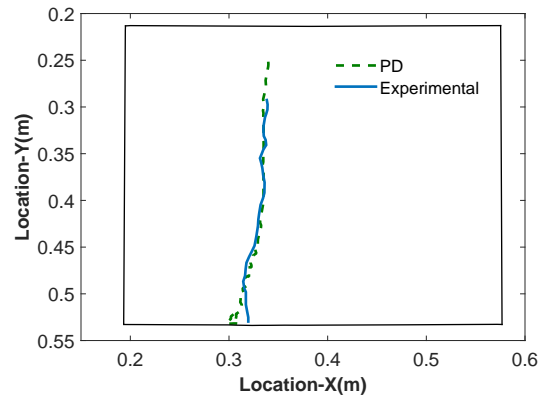

Figure 12: Numerical and experimental crack trajectories

Therefore, with the guidance of the coefficient distributions, the OSB PD is introduced in a local rectangular region with poor correlation to achieve the damage evolution and crack propagation. The concrete material properties and the pixel information of DIC images for this problem are listed in the Tab. 1. The region is uniformly discretized with grid spacing of Δx=2.5 mm, the horizon size is set as $\delta = 3\,\Delta x$, and the time step is adopted as $\Delta t = 1 \times 10^{-7}s$ in the explicit time integration algorithm. Also, the critical stretch is 1.5×10^{-3}.

The peridynamic simulation can clearly capture the whole process of damage accumulation, crack initiation and propagation and the final failure pattern of the concrete specimen. Fig. 11 presents the surface morphologies of four typical deformation states respectively under the loading level of 0 kN, 3.34 kN, 7.78 kN and 10.00 kN, in which the left

column is the experimental results and the right column is the PD predicted damage distribution. Comparing Fig. 11(c) with Fig. 11(a) and Fig. 11(b), one cannot discover obvious distinctions and surface micro-cracks in the experimental results with naked eyes. Fortunately, the OSB PD prediction can show the process of damage evolution and crack propagation. Specifically, there was no damage under the loading level of 3.34 kN; nevertheless, the damage accumulated significantly, leading to the formation of a damage band when the load reached to 7.78 kN, as shown in Fig. 11(c); moreover, the crack propagated gradually to form an apparent macro-crack as the load increased from 7.78 kN to 10.00 kN, as shown in Fig. 11(d). Furthermore, the numerical and experimental crack trajectories are plotted together in Fig. 12, which are in good consistent, demonstrating the capability of the integrated DIC and OSB PD approach. Our method not only improves the accuracy of DIC results with non-smooth or discontinuous deformation, but also increases the computational efficiency of PD simulations by simply extracting boundary conditions from DIC experiment results.

In addition, the PD strain components under different loads are compared with the local strain components from DIC technique, as shown in Fig. 13. The PD strains outside the crack are comparable with the local strains, while the PD strains near and inside the crack are different from the DIC results.
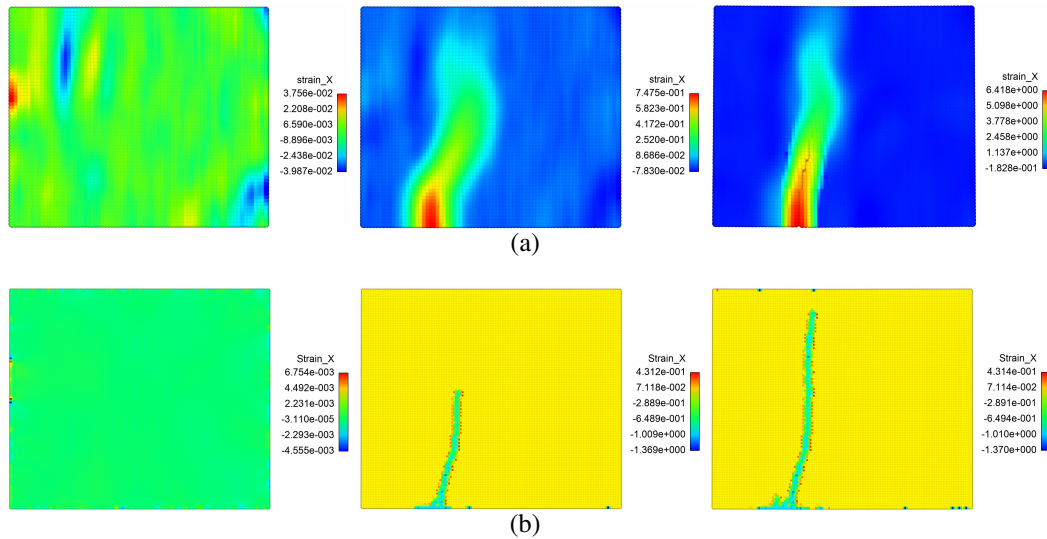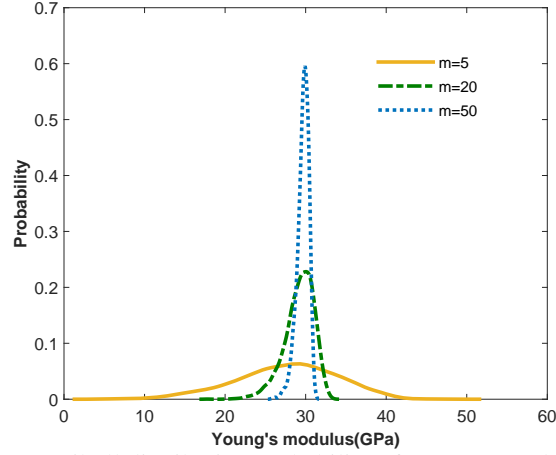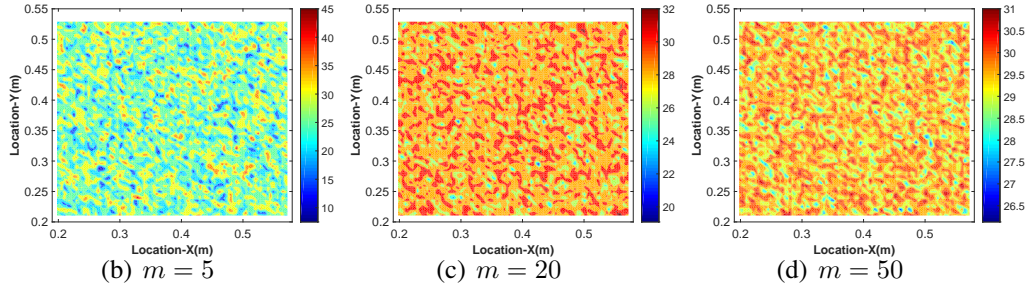

Figure 13: Comparison of strains obtained from (a) DIC measurement and (b) PD prediction under different loads of 3.34 kN, 7.78 kN and 10.00 kN

(a) Weibull distribution probability of Young's modulus

(b) $m = 5$ (c) $m = 20$ (d) $m = 50$

Figure 14: Random Young's modulus in concrete specimens with different homogeneous indexs m

5.2.3 Fracture simulations considering concrete heterogeneity

Heterogeneity is a typical characteristic of concrete materials. Therefore, it is necessary to investigate the effect of material heterogeneity on crack initiation and propagation. Here, the material parameters are assumed to satisfy the Weibull distribution [Tang and Yang (2012); Wang, Zhou and Shou (2017)]

$$\varphi(a) = \frac{m}{a_0} \left(\frac{a}{a_0} \right)^{m-1} \exp\left[-\left(\frac{a}{a_0} \right)^m \right], \tag{12}$$

where $\varphi(a)$ is a statistical distribution density function, a is the mechanical property, such as Young's modulus, a_0 is the average value of the mechanical property and m is the homogeneity level index, which indicates the heterogeneity of a material. The larger the value of m, the more homogeneous the material.
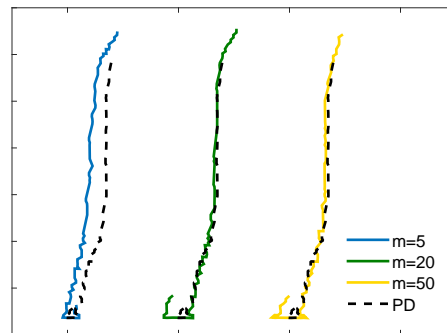
Figure 15: Numerical and experimental crack trajectories

Fig. 14(a) shows the Weibull distribution of Young's modulus in concrete specimens with the index value of $m = 5$, 20 and 50. Also, it can be obtained from Figs. 14(b)-14(d) that the concrete specimen becomes strongly heterogeneous with $m = 5$. Three OSB PD simulations with $m = 5$, 20 and 50 are conducted to get the final crack paths, which are depicted together with the experimental result in Fig. 15. Although external loading conditions are same for those simulations and the crack initiation positions are always close, the crack propagation and the final crack trajectories are slightly different due to the effect of material heterogeneity.

6 Conclusion

In this paper, a new DIC algorithm based on peridynamics is proposed, which can generate high-quality displacements for problems involving cracks and other discontinuities. The combination of DIC technique and peridynamics provided a viable approach for advanced study of damage in brittle materials, which extends DIC to previously difficult or intractable problems. The ordinary state-based peridynamics to characterize material damage from DIC full-field displacements shows great potential. The algorithm is demonstrated to be robust by analyzing the failure of a compact tension specimen of aluminum alloy and a static three-point bending concrete beam. It also reveals that the coupled DIC and PD strategy can be utilized to predict the damage evolution and invisible micro-crack initiation and propagation of materials and structures before macro-crack forms.

References

Bie, Y.; Cui, X.; Li, Z. (2018): A coupling approach of state-based peridynamics with node-based smoothed finite element method. *Computer Methods in Applied Mechanics and Engineering*, vol. 331, pp. 675-700.

Caggegi, C.; Chevalier, L.; Pensée, V.; Cuomo, M. (2016): Strain and shear stress fields analysis by means of digital image correlation on CFRP to brick bonded joints fastened by fiber anchors. *Construction and Building Materials*, vol. 106, pp. 78-88.

Cai, Y.; Zhang, Q.; Yang, S.; Fu, S.; Wang, Y. (2016): Experimental study on three-dimensional deformation field of portevin-le chatelier effect using digital image correlation. *Experimental Mechanics*, vol. 56, no. 7, pp. 1243-1255.

Chu, T.; Ranson, W.; Sutton, M. A. (1985): Applications of digital-image-correlation techniques to experimental mechanics. *Experimental Mechanics*, vol. 25, no. 3, pp. 232-244.

Conradi, J.; Turner, D.; Becker, T. (2014): Characterising damage in structural materials using digital image correlation and peridynamics. *South African Conference on Computational and Applied Mechanics*, pp. 238-242.

Dipasquale, D.; Sarego, G.; Zaccariotto, M.; Galvanetto, U. (2017): A discussion on failure criteria for ordinary state-based peridynamics. *Engineering Fracture Mechanics*, vol. 186, pp. 378-398.

Farahani, B. V.; Tavares, P. J.; Belinha, J.; Moreira, P. (2018): Compact tension fracture specimen: experimental and computational implementations on stress intensity factor. *Journal of Strain Analysis for Engineering Design*, vol. 53, no. 8, pp. 630-647.

Gao, Y.; Oterkus, S. (2019): Fully coupled thermomechanical analysis of laminated composites by using ordinary state based peridynamic theory. *Composite Structures*, vol. 207, pp. 397-424.

Grytten, F.; Daiyan, H.; Polanco-Loria, M.; Dumoulin, S. (2009): Use of digital image correlation to measure large-strain tensile properties of ductile thermoplastics. *Polymer Testing*, vol. 28, no. 6, pp. 653-660.

Gu, X.; Madenci, E.; Zhang, Q. (2018): Revisit of non-ordinary state-based peridynamics. *Engineering Fracture Mechanics*, vol. 190, pp. 31-52.

Gu, X.; Zhang, Q.; Madenci, E. (2019): Refined bond-based peridynamics for thermal diffusion. *Engineering Computations*, vol. 36, no. 8, pp. 2557-2587.

Gu, X.; Zhang, Q.; Xia, X. (2017): Voronoi-based peridynamics and cracking analysis with adaptive refinement. *International Journal for Numerical Methods in Engineering*, vol. 112, no. 13, pp. 2087-2109.

Han, F.; Lubineau, G.; Azdoud, Y.; Askari, A. (2016): A morphing approach to couple state-based peridynamics with classical continuum mechanics. *Computer methods in applied mechanics and engineering*, vol. 301, pp. 336-358.

Huang, D.; Lu, G.; Qiao, P. (2015): An improved peridynamic approach for quasi-static elastic deformation and brittle fracture analysis. *International Journal of Mechanical Sciences*, vol. 94, pp. 111-122.

Imachi, M.; Tanaka, S.; Bui, T. Q.; Oterkus, S.; Oterkus, E. (2019): A computational approach based on ordinary state-based peridynamics with new transition bond for dynamic fracture analysis. *Engineering Fracture Mechanics*, vol. 206, pp. 359-374.

Jerabek, M.; Major, Z.; Lang, R. (2010): Strain determination of polymeric materials using digital image correlation. *Polymer Testing*, vol. 29, no. 3, pp. 407-416.

Jiang, Y.; Jin, Z.; Zhao, T.; Chen, Y.; Chen, F. (2017): Strain field of reinforced concrete under accelerated corrosion by digital image correlation technique. *Journal of Advanced Concrete Technology*, vol. 15, no. 7, pp. 290-299.

Justin, B.; Antonia, A. (2015): Ncoor v1.2. http://www.ncorr.com/index.php/contact.

Lall, P.; Kulkarni, M.; Angral, A.; Panchagade, D.; Suhling, J. (2010): Digital-image correlation and XFEM based shock-reliability models for leadfree and advanced interconnects. *Proceedings 60th Electronic Components and Technology Conference*, pp. 91-105.

Le, Q.; Chan, W.; Schwartz, J. (2014): A two-dimensional ordinary, state-based peridynamic model for linearly elastic solids. *International Journal for Numerical Methods in Engineering*, vol. 98, no. 8, pp. 547-561.

Lei, D.; Hou, F.; Gong, X. (2012): Investigation of deformation at the grain scale in polycrystalline materials by coupling digital image correlation and digital microscopy. *Experimental Techniques*, vol. 36, no. 2, pp. 24-31.

Lei, D.; Yang, L.; Xu, W.; Zhang, P.; Huang, Z. (2017): Experimental study on alarming of concrete micro-crack initiation based on wavelet packet analysis. *Construction and Building Materials*, vol. 149, pp. 716-723.

Liu, X.; He, X.; Wang, J.; Sun, L.; Oterkus, E. (2018): An ordinary state-based peridynamic model for the fracture of zigzag graphene sheets. *Proceedings of the Royal Society A: Mathematical, Physical and Engineering Sciences*, vol. 474, no. 2217.

Madenci, E.; Barut, A.; Futch, M. (2016): Peridynamic differential operator and its applications. *Computer Methods in Applied Mechanics and Engineering*, vol. 304, pp. 408-451.

Madenci, E.; Dorduncu, M.; Barut, A.; Futch, M. (2017): Numerical solution of linear and nonlinear partial differential equations using the peridynamic differential operator. *Numerical Methods for Partial Differential Equations*, vol. 33, no. 5, pp. 1726-1753.

Murienne, B. J.; Chen, M. L.; Quigley, H. A.; Nguyen, T. D. (2016): The contribution of glycosaminoglycans to the mechanical behaviour of the posterior human sclera. *Journal of the Royal Society Interface*, vol. 13, no. 119, 20160367.

Oterkus, E.; Madenci, E.; Weckner, O.; Silling, S.; Bogert, P. et al. (2012): Combined finite element and peridynamic analyses for predicting failure in a stiffened composite curved panel with a central slot. *Composite Structures*, vol. 94, no. 3, pp. 839-850.

Pan, B.; Yu, L.; Wu, D. (2015): Thermo-mechanical response of superalloy honeycomb sandwich panels subjected to non-steady thermal loading. *Materials & Design*, vol. 88, pp. 528-536.

Parks, M. L.; Seleson, P.; Plimpton, S. J.; Silling, S. A.; Lehoucq, R. B. (2011): Peridynamics with lammps: a user guide, v0. 3 beta. *Sandia Report SAND 2011-8523, Sandia National Laboratories*.

Poissant, J.; Barthelat, F. (2010): A novel' subset splitting' procedure for digital image correlation on discontinuous displacement fields. *Experimental Mechanics*, vol. 50, no. 3, pp. 353-364.

Réthoré, J.; Hild, F.; Roux, S. (2008): Extended digital image correlation with crack shape optimization. *International Journal for Numerical Methods in Engineering*, vol. 73, no. 2, pp. 248-272.

Réthoré, J.; Roux, S.; Hild, F. (2007): From pictures to extended finite elements: extended digital image correlation (x-dic). *Comptes Rendus Mécanique*, vol. 335, no. 3, pp. 131-137.

Silling, S. A. (2000): Reformulation of elasticity theory for discontinuities and long-range forces. *Journal of the Mechanics and Physics of Solids*, vol. 48, no. 1, pp. 175-209.

Silling, S. A.; Askari, E. (2005): A meshfree method based on the peridynamic model of solid mechanics. *Computers & Structures*, vol. 83, no. 17-18, pp. 1526-1535.

Silling, S. A.; Epton, M.; Weckner, O.; Xu, J.; Askari, E. (2007): Peridynamic states and constitutive modeling. *Journal of Elasticity*, vol. 88, no. 2, pp. 151-184.

Sutton, M.; Wolters, W.; Peters, W.; Ranson, W.; McNeill, S. (1983): Determination of displacements using an improved digital correlation method. *Image and Vision Computing*, vol. 1, no. 3, pp. 133-139.

Tang, C. A.; Yang, Y. F. (2012): Crack branching mechanism of rock-like quasi-brittle materials under dynamic stress. *Journal of Central South University*, vol. 19, no. 11, pp. 3273-3284.

Tung, S. H.; Shih, M. H.; Kuo, J. C. (2010): Application of digital image correlation for anisotropic plastic deformation during tension testing. *Optics and Lasers in Engineering*, vol. 48, no. 5, pp. 636-641.

Turner, D. (2014): Peridynamics-based digital image correlation algorithm suitable for cracks and other discontinuities. *Journal of Engineering Mechanics*, vol. 141, no. 2, 04014115.

Wang, Y.; Zhou, X.; Shou, Y. (2017): The modeling of crack propagation and coalescence in rocks under uniaxial compression using the novel conjugated bond-based peridynamics. *International Journal of Mechanical Sciences*, vol. 128, pp. 614-643.

Warren, T. L.; Silling, S. A.; Askari, A.; Weckner, O.; Epton, M. A. et al. (2009): A non-ordinary state-based peridynamic method to model solid material deformation and fracture. *International Journal of Solids and Structures*, vol. 46, no. 5, pp. 1186-1195.

Zhang, H.; Qiao, P. (2018): An extended state-based peridynamic model for damage growth prediction of bimaterial structures under thermomechanical loading. *Engineering Fracture Mechanics*, vol. 189, pp. 81-97.

Zhou, X.; Shou, Y.; Berto, F. (2018): Analysis of the plastic zone near the crack tips under the uniaxial tension using ordinary state-based peridynamics. *Fatigue & Fracture of Engineering Materials & Structures*, vol. 41, no. 5, pp. 1159-1170.